ACS APPLIED ENERGY MATERIALS
Cite This: ACS Appl. Energy Mater. XXXX, XXX, XXX−XXX
Article
www.acsaem.org

Beneficial CuO Phase Segregation in the Ternary p-Type Oxide Photocathode $CuBi_2O_4$

Zemin Zhang,[†,‡] Sarah A. Lindley,[‡] Rohan Dhall,[∥] Karen Bustillo,[∥] Weihua Han,[†] Erqin Xie,[†] and Jason K. Cooper*[,‡,§]

[†]School of Physical Science and Technology, Lanzhou University, Lanzhou 730000, China
[‡]Joint Center for Artificial Photosynthesis, Lawrence Berkeley National Laboratory, Berkeley, California 94720, United States
[§]Chemical Sciences Division, Lawrence Berkeley National Laboratory, Berkeley, California 94720, United States
[∥]National Center for Electron Microscopy, Molecular Foundry, Lawrence Berkeley National Laboratory, Berkeley, California 94720, United States

Supporting Information

ABSTRACT: Assessing the intrinsic material performance of emerging copper-based ternary oxide photocathode candidate materials such as $CuBi_2O_4$ (CBO) has been challenging due to the formation of phase-segregated domains in films with stoichiometric nonideality. However, we find films with CuO phase segregation demonstrate improved photoelectrochemical (PEC) performance, the origin of which inspired this deeper investigation. Uniform and compact CBO thin films with Bi:Cu ratios of 2.10, 1.97, 1.78, and 1.38 were grown by spin-coating. Although CuO was detected by Raman and X-ray diffraction in the 1.38 film only, high resolution energy-dispersive X-ray spectroscopy mapping revealed the presence of 10−20 nm CuO particles at the CBO/FTO interface in the 1.38, 1.78, and 1.97 samples. The greater number of CuO particles in the 1.38 sample resulted in a 25% enhancement in incident photon-to-current efficiency performance but could not be attributed to CuO-related light absorption. X-ray photoelectron spectroscopy characterization of the type-II band alignment was used to confirm that the particles behave as hole-selective contacts. The presence of nanoparticulate heterojunctions improves carrier collection of low diffusion length holes, enhancing the performance of the heterojunction beyond that of a fully planar derivative.

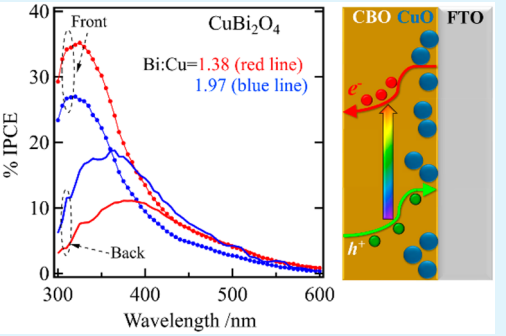

KEYWORDS: *photocathode, copper-based ternary oxide, phase segregation, heterojunction, EDX mapping, carrier collection*

1. INTRODUCTION

With the limited availability of p-type metal-oxide-based photocathode materials for applications such as CO_2 reduction, significant efforts are dedicated to finding new materials with improved stability, ideal bandgaps, and band energetics at the correct chemical potentials for the desired chemical reactivity. Many such emerging p-type materials are copper-based bimetallics based on the well-known p-type semiconductor cuprous oxide (Cu_2O).[1−9] One such example is $CuBi_2O_4$ (CBO), which has a suitable band gap for sunlight harvesting (1.5−1.8 eV) and a relatively positive valence band potential, making it an attractive candidate for CO_2 reduction.[10−19] To make meaningful advances toward understanding the fundamental material properties and thereby identify performance-limiting factors, the development of high-quality material of known composition and phase is necessary. Notably with ternary oxides, device properties can vary significantly depending on the ratio of the component elements.[1−3,9,20] Films are commonly annealed at temperature >500 °C, which can result in sublimation of select elements,[9,21] making phase purity and ideal stoichiometry difficult to achieve. Indeed, literature reports commonly demonstrate CBO containing cupric oxide (CuO) phase impurities.[22−24]

Significant effort is spent to ensure synthesis methods produce phase pure materials, often determined by X-ray diffraction (XRD) and Raman spectroscopy. As a consequence of these efforts, it is common to test the functional performance of a variety of compositions, thereby achieving a feedback loop between synthesis and performance.[1,20] Often, nonideal stoichiometries demonstrate improved performance which is attributed to interstitial or substitutional "doping". In reality, the composition of many alloys varies from the ideal stoichiometry by several percent, which can lead to phase segregation.[22−24] However, phase uniformity can be challenging to detect, particularly with amorphous or nanoscale impurities. The impact of phase segregated domains can range from deleterious (charge trapping, increasing recombination, or parasitic light absorption) to beneficial (increased

Received: February 12, 2019
Accepted: May 8, 2019
Published: May 8, 2019

DOI: 10.1021/acsaem.9b00297
ACS Appl. Energy Mater. XXXX, XXX, XXX−XXX

light scattering, selective charge transport, or improved catalytic activity). Therefore, the size and location of the domains, their impact on light harvesting efficiency, and the electronic band alignments at the heterojunction must be known to deconvolve intrinsic material properties from unintentional cooperative benefits of phase segregation.

In this investigation, we utilized spin coating to achieve uniform, compact, and controllable growth of CBO with good precision and reproducibility of the resultant Bi:Cu stoichiometry. When copper concentration was increased and Bi:Cu ratio decreased from ideality, phase-segregated CuO was identified by grazing incidence (GI)-XRD and Raman spectroscopy, and photoelectrochemical (PEC) performance showed significant improvement. To understand the effects of this phase segregation, high resolution cross-section energy-dispersive X-ray spectroscopy (EDX) mapping was applied to investigate the location, size, and amount of CuO domains. Interestingly, CuO domains were found in most samples, even those approaching the conventionally ideal 2:1 Bi:Cu ratio. Combining structural information with PEC performance and band alignment analysis, the CuO particles are revealed to be crucial components of the photocathode heterojunction, acting as hole selective nanoscale contacts, improving charge collection efficiency, and thereby enhancing PEC performance. Such nanoparticle heterojunctions can be applied to other materials where low mobility carriers limit performance.

2. EXPERMENTAL SECTION

2.1. Preparation of CBO Films. $CuBi_2O_4$ thin films were fabricated on fluorine-doped tin oxide (FTO) glass substrates by spin coating. Bismuth(III) nitrate pentahydrate (Sigma-Aldrich, ≥98%) and copper(II) nitrate trihydrate (Sigma-Aldrich, ≥99%) in various Bi:Cu mole ratios were dissolved in 2-methoxyethanol (Sigma-Aldrich, ReagentPlus, ≥99%) as the precursor. Triethyl orthoformate (TEOF, Sigma-Aldrich, anhydrous, 98%) was used as a water scavenger to stabilize the bismuth ions and avoid precipitation (volume ratio of 2%). The FTO glass substrates (Sigma-Aldrich, 50 × 50 × 2 mm, ∼7 ohm/square) were thoroughly washed with detergent, isopropanol, and deionized water, dried with a nitrogen gun, and treated for 20 min in a UV-ozone cleaner (Jelight Model 42). The precursor solution was applied uniformly to the substrate, filtered through a 0.25 μm PTFE filter (Thermo Scientific), and spun at 1000 rpm for 30 s on a Laurell Technologies spin coater with an acceleration rate of 150 rpm/s. After spin coating, substrates were annealed for 20 min at 550 °C in a muffle furnace. This procedure (i.e. spin coating followed by short annealing) was repeated five times. After the final spin coating cycle, the substrate was annealed for 2 h at 550 °C to achieve the final CBO samples. For comparison, a CuO thin film sample was fabricated on FTO glass by the same method but excluding Bi. CuO/CBO samples were prepared by one cycle of CuO deposition followed by five cycles of CBO deposition, as previously described.

2.2. Characterization. The crystalline structure of the samples was analyzed by GIXRD with a Rigaku Smartlab diffractometer using Cu Kα radiation. The incident angle was fixed at 0.5°, and the detector angle was scanned between 25° and 75°. The elemental composition of the films was determined with an inductively coupled plasma mass spectrometer (7900 ICP-MS, Agilent) and further confirmed by Rutherford backscattering spectrometry (RBS). For ICP-MS, the thin films were digested in 1 mL of trace metals grade concentrated nitric acid (Sigma-Aldrich, 225711) and then diluted to 5 mL with ultrapure water. Resultant solutions were further diluted with 2% HNO_3 to obtain a sample concentration within the range covered by the calibration curve (1−1000 ppb). One ppm W and Ge were used as internal standards. For RBS, He ions were accelerated to 3040 keV on a 5SDH pelletron tandem accelerator manufactured by National Electrostatics Corporation with a sample tilt of 30−60° and backscattered ions were detected at an angle of 165° using a Si surface barrier detector. Data fitting was performed with SIMNRA software. Sample surface morphology was inspected using a scanning electron microscope (SEM, Quanta FEG 250, FEI). Raman spectra were recorded using a confocal Raman microscope (LabRam HR, Horiba Jobin Yvon) with a 532 nm laser source. The transmittance and reflectance spectra of the samples were recorded at an 8° angle of incidence using a UV−vis spectrometer equipped with an integrating sphere (SolidSpec 3700, Shimadzu). The cross-section EDS-mapping of the samples was inspected by using transmission electron microscopy (FEI TitanX 60−300 operating at 200 kV) with a large solid angle EDS detector. Cross-section sample preparation was performed using a Multiprep tool followed by Ar ion milling to thin the samples.

Photothermal deflection spectroscopy (PDS) was collected on a home-built system, in which monochromatic light from a laser stimulated light source (EQ-77, Enertiq) was modulated with an optical shutter and used to excite the sample, which was immersed in perfluorohexane. The grazing probe beam was provided by a stabilized HeNe laser, and its position was detected with a position sensitive detector, amplified and filtered with a current preamplifier, and then recorded with a lock-in amplifier.

Surface photovoltage (SPV) was conducted at room temperature using a Kelvin probe (Kelvin Probe S, Besocke Delta Phi GmbH) by measuring the contact potential difference (CPD) with or without illumination: SPV = ΔCPD = $CPD_{light} - CPD_{dark}$. A 340 nm LED (M340L4, ThorLabs) with about 10 mW cm^{-2} power density was used as the light source. The Kelvin probe measurements were conducted using a piezoelectrically driven gold grid with a diameter of 3 mm. The CPD is given by: $V_{CPD} = \phi_{CBO} - \phi_{ref}$, where ϕ_{CBO} and ϕ_{ref} are the work function of CBO film and gold reference electrode, respectively.

X-ray photoelectron spectroscopy (XPS) data were acquired by a Kratos Axis Ultra spectrometer, using a monochromatic Al Kα source (hv = 1486.69 eV). The work function was determined from the secondary electron cutoff by applying a −10 V bias voltage to the sample. Spectral positions were calibrated using adventitious alkyl carbon signals by shifting the C 1s peak to 284.8 eV.

2.3. Photoelectrochemical Characterization. PEC measurements were performed with a Biologic SP-300 potentiostat using a three-electrode configuration with a Pt counter electrode and 3 M Ag/AgCl reference electrode at a scan rate of 50 mV/s. The CBO working electrode was prepared by connecting the CBO/FTO sample to copper wire using silver epoxy and inserting into a glass tube. The sample edge and connection area were protected by chemically resistant epoxy. A photograph of the completed working electrode is provided in Figure S1. Potassium bicarbonate (0.1 M, Sigma-Aldrich, ≥99.95%) and sodium persulfate (0.1 M, Sigma-Aldrich, Reagent, ≥98%) were used as electrolyte at pH 8.2. Here, sodium persulfate works as an electron scavenger. Simulated AM 1.5G solar illumination is provided by a solar simulator (16S-300-002, Solar Light) with a flux of 100 mW/cm^{-2}, as determined by a calibrated Newport Si PV module. All reported potentials were converted to the reversible hydrogen electrode (RHE) scale using the following relation (1):

$$E_{RHE} = E_{Ag/AgCl} + 0.21V + (0.059 \times pH) \quad (1)$$

Applied bias photocurrent efficiency (ABPE) was calculated and compared based on the $J-V$ response of the samples using the following relation (2):

$$ABPE = \frac{(E_{S_2O_8} - E_{applied})(V_{RHE}) \times j_{ph}(mAcm^{-2})}{P_{total}(mW/cm^{-2})} \quad (2)$$

Here, $E_{S_2O_8}$ is the reduction potential for sodium persulfate, which was measured in the same three-electrode system by using CBO as the working electrode in N_2-purged potassium bicarbonate (0.1 M) with or without sodium persulfate (0.1 M). $E_{applied}$ is the applied potential, and j_{ph} is the related photocurrent density. P_{total} is the incident light

DOI: 10.1021/acsaem.9b00297
ACS Appl. Energy Mater. XXXX, XXX, XXX−XXX

density, which was set to 100 mW/cm^{-2}, as determined by a calibrated Newport Si PV module.

The incident photon-to-current efficiency (IPCE) was measured in the same electrolyte as used for PEC testing at 5 nm intervals between 280 and 700 nm. A 150 W Xe lamp (M6255, Newport) combined with a holographic grating monochromator (CS-130, Oriel Instruments) as well as a broadband continuous light bias supplied by a high-power light-emitting diode (GCS-6500-15-A0510, Mightex) were used to illuminate the front-side as well as back side of the CBO sample in a PEC cell. The differences in photocurrent and dark current responses at individual wavelengths were acquired by a Gamry Reference 600 potentiostat. The power of the monochromatic light was cocollected by recording the photocurrent response from a calibrated Si photodiode.

APCE was calculated by dividing IPCE by film absorbance, which was measured with a UV−vis spectrometer using the following relation:

$$\mathrm{APCE}(\lambda) = \mathrm{IPCE}(\lambda)/[1 - T(\lambda) - R(\lambda)] \quad (3)$$

where T represents transmittance and R represents reflectance.

3. RESULTS AND DISCUSSION

CBO films were prepared by spin coating and annealing precursor solutions with Bi:Cu mole ratios of 2.4, 2.2, 2.0, and 1.5. ICP-MS of the resultant films revealed final Bi:Cu ratios of 2.10, 1.97, 1.78, and 1.38, respectively. These ratios were confirmed with RBS measurement, and all values are tabulated in Table 1. The concentration of Bi in the film was reduced after annealing, which suggested sublimation of Bi during the annealing process. As a result, our annealing times and temperature were carefully controlled. Further studies are warranted to relate annealing time to Bi:Cu and PEC performance. The ICP-MS ratios are used as sample IDs for the following analysis and discussions.

Table 1. Stoichiometry and Film Thickness for CBO Films with Various Bi:Cu Ratios

stoichiometry (Bi:Cu)				
sample	precursor	ICP-MS	RBS	thickness (nm)[a]
2.10	2.4	2.10	2.08 ± 0.04	152 ± 5
1.97	2.2	1.97	1.93 ± 0.03	198 ± 5
1.78	2.0	1.78	1.77 ± 0.02	210 ± 5
1.38	1.5	1.38	1.39 ± 0.04	195 ± 5

[a]Film thickness is calculated from RBS data; film density is 8.5 g/cm^3 and assumed to be similar for all samples.

SEM images of each sample are shown in Figure 1a−d, revealing grain sizes on the order of ∼200 nm. Cross-sectional SEM (Figure S2, 1.97) shows the grains are contiguous and continuous. Film thickness values are also reported in Table 1. GI-XRD patterns shown in Figure 1e reveal all samples are of Kusachiite phase (JCPDS 42-0334), and the Raman spectra in Figure 1f demonstrate no secondary phase.[25] However, characteristic CuO peaks appear in the GI-XRD and Raman spectra for the 1.38 sample, suggesting phase segregation in the least ideal film.

To characterize the size, extent, and location of the segregated CuO domains, we employed transmission electron microscopy (TEM) with high resolution EDX mapping to probe the cross-section of the 1.38 and 1.97 samples. The 1.97 sample was chosen for comparison, as it is of a similar thickness to the 1.38 film and closest to the conventionally ideal 2:1 Bi:Cu ratio. The resultant EDX spectrum (Figure S3) indicates the elemental purity of both samples. Three different cross-section regions are shown in Figure 1 (h) for the 1.97 film and (i) for the 1.38 film. As expected from the Raman data, Cu-rich regions of the 1.38 film are clearly visible and concentrated at the FTO/CBO interface. Surprisingly, similar Cu-rich regions are also evident in the 1.97 sample, although to a lesser extent. For both films, the size of these regions was measured to be 10−20 nm in diameter. It is likely these regions arise from CuO deposits, which were plentiful enough in the 1.38 film to be detectable with Raman and XRD but sparse enough in the 1.97 film to elude such detection. This finding stresses the importance of high-resolution elemental mapping in characterizing phase-segregated films. Relying on Raman and XRD data alone would have resulted in mischaracterization of the 1.97 film with regard to the presence of CuO deposits. It should be noted that Cu-rich regions were not observed in the EDX mapping of the 2.10 sample (Figure S4), indicating that a Bi concentration in excess of ideality is necessary for phase purity in this system.

In assessing the films as PEC photocathode materials, higher performance was achieved with lower Bi:Cu ratio. The $J-V$ responses for the 1.97 and 1.38 films are compared in Figure 1g, and the related applied bias photo conversion efficiencies (ABPE), as measured under AM 1.5G illumination at 100 mW cm^{-2} (0.1 M $KHCO_3$), are displayed Figure S5c. Once again, the 1.97 and 1.38 samples are chosen for comparison due to their similar film thicknesses. For these measurements, an electron scavenger (0.1 M $Na_2S_2O_8$) was added to the electrolyte to study the intrinsic properties of the materials without the effect of surface activity.[10] Lowering the Bi:Cu ratio from 1.97 to 1.38 resulted in an increase in the photocurrent from 0.82 to 1.17 mAcm^{-2} at 0.58 V_{RHE}, a positive shift in the onset potential from 1.218 to 1.244 V_{RHE} (taken at 1 μA cm^{-2} of photocurrent), and an increase in maximum ABPE from 0.39 to 0.55% under 0.58 V_{RHE} (Figure S5c). The ABPE was determined using eq 2 with the reduction potential for persulfate determined to be 0.12 V_{RHE} (Figure S5b). To further confirm this result, the 2.10 and 1.78 samples were also compared. The $J-V$ response (Figure S5a) and related ABPE (Figure S5c) show similar dependence. Therefore, the enhancement in PEC performance achieved with a decrease in Bi:Cu ratio is well correlated to both the appearance and prevalence of interfacial CuO deposits. To understand the reason for the correlation, we must identify the role of this segregated phase.

One possible explanation for the improved PEC performance could be that additional light harvesting by the CuO particles and subsequent transport of electrons through the CBO layer to the semiconductor/electrolyte interface contributes to increased photocurrent. Indeed, the UV−vis spectra in Figure 2a show an increase in the absorption throughout the visible and into the near IR region of the spectrum for the 1.38 film. Because the difference in absorption does not arise from a difference in CBO thickness, we can attribute the increased absorption to the presence of the secondary CuO phase. The transmittance and reflectance spectra shown in Figure S6 confirm that sample thicknesses are nearly identical for these films (based on the thin film interference). To support this conclusion, the absorption coefficient for each film was determined with photothermal deflection spectroscopy (PDS), which detects the heat dissipated from the sample through nonradiative recombination. Absorption coefficients for a CuO thin film, made by the same spin-coating method

DOI: 10.1021/acsaem.9b00297
ACS Appl. Energy Mater. XXXX, XXX, XXX−XXX

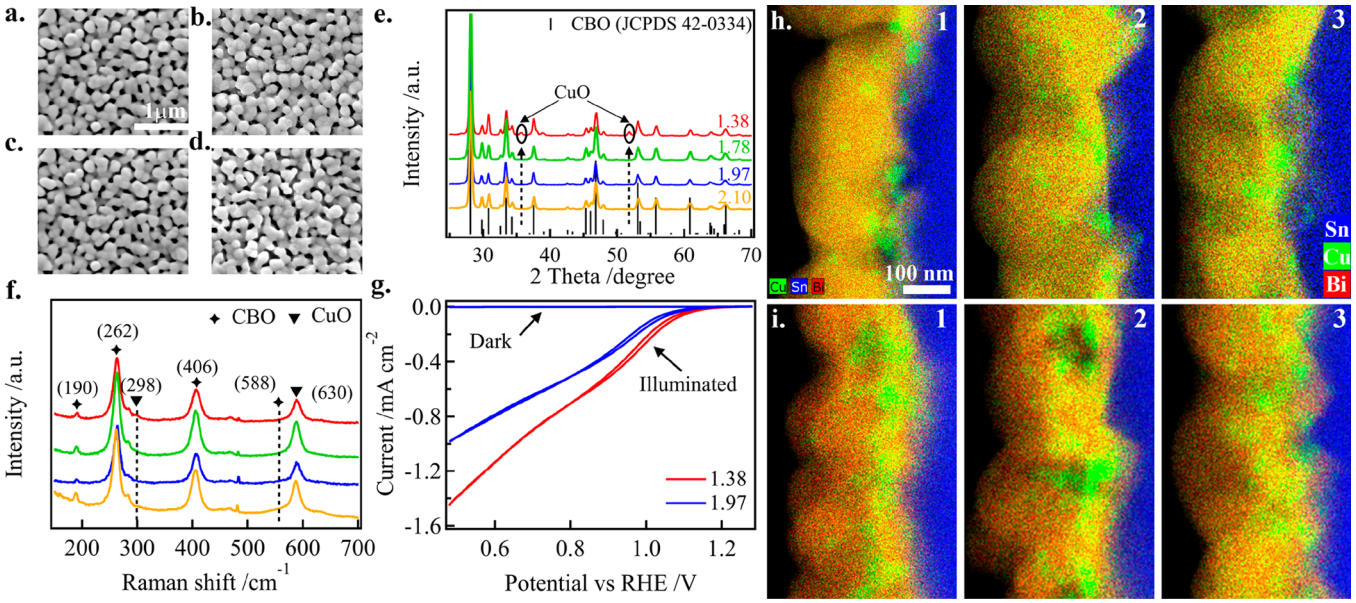

Figure 1. SEM images of CBO films on FTO glass substrate with Bi:Cu ratio of (a) 1.38, (b) 1.78, (c) 1.97, and (d) 2.10. (e) GI-XRD and (f) Raman spectra of the CBO films with ratio as indicated. (g) The $J-V$ response of CBO samples under front AM 1.5 illumination at 100 mW cm^{-2} in 0.1 M $KHCO_3$ with 0.1 M $Na_2S_2O_8$ (pH 8.2). Cross-section element mapping of CBO samples with Bi:Cu ratio of (h) 1.97 and (i) 1.38. EDX maps are constructed from the Cu−K edge, Sn-L edge, and Bi-L edge.

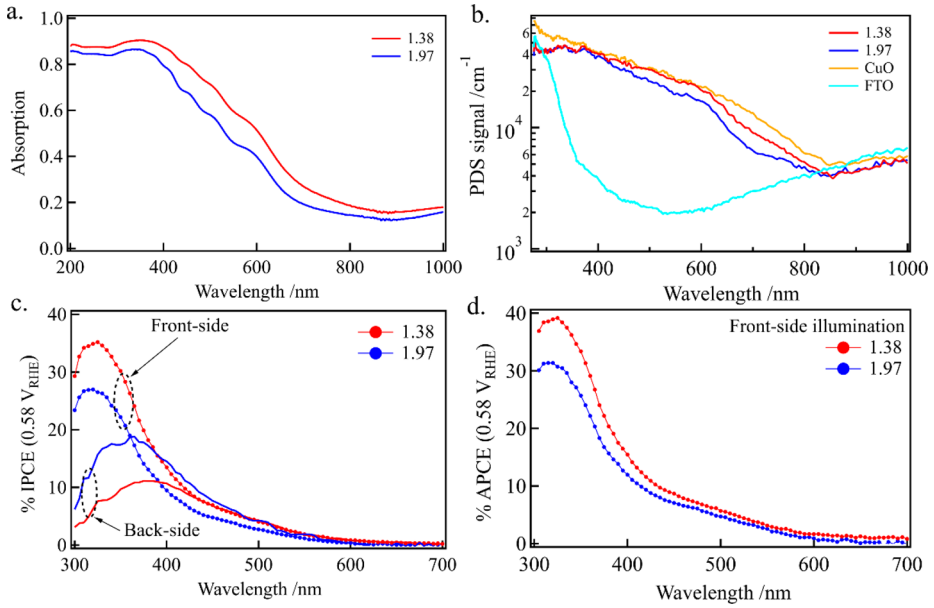

Figure 2. (a) Absorption spectra and (b) PDS absorption coefficient for CBO with Bi:Cu ratio of 1.38 (red) and 1.97 (blue). PDS for CuO (orange) and FTO glass substrate (light blue) are provided for comparison. (c) Front- and back-side illuminated %IPCE and (d) front-side illuminated %APCE spectra of CBO deposited on FTO glass with Bi:Cu ratio of 1.38 (red) and 1.97 (blue), collected at 0.58 V_{RHE}.

with omission of the Bi precursor as well as FTO are provided for comparison. As shown in Figure 2b, CuO shows a higher absorption coefficient than CBO, and absorption in the wavelength range of 600−800 nm is similar to that of the 1.38 CBO sample, supporting the conclusion that enhanced absorption is afforded by the presence of CuO particles. It should be noted that the weak absorption in the infrared arises from free carrier absorption in the highly doped FTO substrate.[26,27]

The light harvesting performance of the films was investigated by IPCE. With front-side illumination and using AM1.5G 1 sun illumination, the calculated current density was 0.57 and 0.71 mA cm^{-2} for the 1.98 and 1.38 samples, respectively, demonstrating an increase of 25% (Figure 2c). Similar behavior was seen in samples 2.1 and 1.78 (Figure S5d). If this improvement is simply due to enhanced light absorption, then APCE data would show similar efficiency between the 1.38 and 1.97 samples.[28] However, APCE also showed improved efficiency from the 1.97 to 1.38 sample, as shown in Figure 2d, suggesting a more complex interrelationship between the CuO particles and CBO. With back side illumination, the trend is reversed, and the 1.97 sample demonstrates the improved IPCE. This result suggests that light absorption in the CuO layer is parasitic, and photocarriers

DOI: 10.1021/acsaem.9b00297
ACS Appl. Energy Mater. XXXX, XXX, XXX−XXX

generated in the particles are not able to contribute meaningfully to PEC performance. These results taken together allow us to hypothesize that CuO is acting as a hole-selective contact, thereby improving charge collection efficiency.[29]

To further investigate the effect of CuO on performance, we fabricated an FTO/CuO/CBO device with a well-defined planar CuO layer. Both CuO and CBO layers were grown sequentially by spin-coating. The performance of the CBO/CuO film was compared to that of a single-layer CBO sample, which was fabricated at the same time using the same process conditions and also had a Bi:Cu ratio of 1.97. High resolution EDX mapping of this device, shown in Figure 3a, indicates a

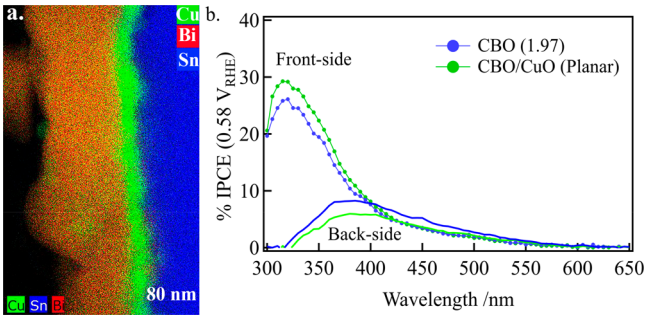

Figure 3. (a) High resolution EDX map for CBO/CuO/FTO with planar heterojunction geometry. EDX map is constructed from the Cu−K edge (green), Sn-L edge (blue), and Bi-L edge (red). (b) IPCE performance of both-side illuminated CBO (1.97, blue) and CBO/CuO (Planar, green) films.

uniform CuO layer (35 nm) at the FTO interface with a uniform compact CBO layer (175 nm) on top of the CuO. Interestingly, no CuO particles were observed in this CBO layer, suggesting the FTO interface acts to nucleate the CuO particles; however, further investigations are necessary to confirm this hypothesis.

With front-side illumination, an increase in the IPCE was observed for the device with the CuO layer (Figure 3b), consistent with our previous results. The increase in IPCE with the CuO layer at the back contact confirms charge transport of photogenerated holes is enabled. On the contrary, if the CuO was unable to transport charge generated in the CBO layer, we should expect a reduction in IPCE. Therefore, we can conclude the CuO acts as a hole transport layer for photogenerated charge from the CBO. With back-side illumination, we again see a suppression of ICPE due to parasitic light absorption in the CuO layer. Considering the planar heterojunction performed less favorably than the heterojunction with a high concentration of interspersed nanoparticles (sample 1.38, Figure 2c), we suggest that holes may be collected more readily in the case of interspersed nanoparticle contact due to the limited hole diffusion length (~10−50 nm, as reported).[21,30] This has also been demonstrated by Kayes et al. for solar cells made from materials with diffusion lengths lower than their optical thickness; the radial p−n junction nanorod geometry was shown to produce significant improvements in efficiencies as compared to that of a planar p−n junction geometry.[31,32]

To confirm that hole transport in the CuO layer is contributing to improved carrier separation efficiency, we measured the surface photovoltage (SPV) by Kelvin probe.[33] The samples were dark-soaked for 24 h to ensure full relaxation of charge prior to measurement. Under front-side illumination, the contact potential difference (CPD) increased by 0.243 and 0.278 V for the 1.97 and 1.38 samples, respectively (Figure S7), which is close to the reported value of 0.21 V.[19] The improvement of 35 meV is consistent with the 26 meV shift in onset potential measured by PEC. The increase in surface photovoltage can be attributed to reduced recombination through spatial separation of injected holes into the CuO particles.

To further support our proposed model, we characterized the band alignments of the materials by XPS using monochromatic Al Kα emission according to previously established methods.[34,35] The work function of the freshly annealed 1.97 sample and CuO films was 4.70 and 5.13 eV, respectively, as determined by secondary electron cutoff in Figure S8. The Fermi level was determined to be 0.89 and 0.26 eV above the valence band, respectively. From analysis of UV−vis spectra, the indirect bandgaps were determined to be 1.63 and 1.5 eV (Figure S9), respectively. From this information, we construct the band energy diagram shown in Scheme 1 before and after the formation of the heterojunction. We confirm the proposed type-II band alignment and conclude that it is energetically favorable for photogenerated holes to be injected from CBO into the valence band of CuO, whereas the conduction band of CuO is inaccessible to CBO photoelectrons.

Scheme 1. Band Energy Diagram Relative to Vacuum for CBO and CuO Determined through a Combination of XPS and UV−Vis (a) before and (b) after Formation of the Heterojunction

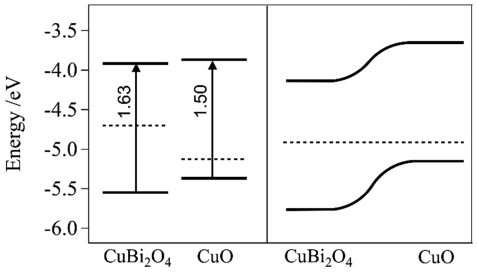

4. CONCLUSION

In summary, a spin-coating method was developed for the growth of high-quality CBO thin films with compact morphology and good precision and reproducibility over the resultant Bi:Cu stoichiometry. The degree of phase purity was found to be sensitive to the Bi:Cu ratio with increase in Cu concentration and resultant decrease in Bi:Cu ratio resulting in an increase in CuO nanoparticle deposits concentrated at the CBO/FTO interface. The CuO particles were on the order of 10−20 nm and were identified in even the most conventionally ideal sample (Bi:Cu = 1.97). We demonstrated that the CuO particles act as hole-selective contacts, improving charge collection efficiency due to the type-II band alignment with CBO. The nanoparticle contact proved to be more advantageous than a planar one due to improved collection efficiency of low mobility holes. The resultant heterojunctions increase the photovoltage by about 35 mV as well as photocurrent by 25% as measured by SPV and PEC. More broadly, this work provides a necessary framework to investigate the effects of stoichiometric nonidealities and related phase segregation in

DOI: 10.1021/acsaem.9b00297
ACS Appl. Energy Mater. XXXX, XXX, XXX−XXX

emerging photoelectrochemical and photovoltaic materials, particularly concerning copper-based ternary oxide semiconductors.

■ ASSOCIATED CONTENT

Supporting Information

The Supporting Information is available free of charge on the ACS Publications website at DOI: 10.1021/acsaem.9b00297.

Optical photo of well-prepared CBO photocathode (Figure S1); stoichiometry, photoelectrochemical characteristics, and surface photovoltage of CBO thin film with different Bi to Cu ratios (Table S1); cross-section SEM image of CBO film on FTO substrate (Figure S2); EDX spectrum of the CBO film with Bi:Cu ratios of 1.97 and 1.38 (Figure S3); cross-section element mapping of CBO samples with Bi:Cu ratio of 2.10 (Figure S4); $J-V$ response, applied bias photocurrent conversation efficiency, and front illuminated incident photocurrent conversation efficiency of CBO films with different copper ratio (Figure S5); transmittance, reflectance spectra of CBO thin film with different Bi/Cu ratio (Figure S6); SPV of CBO thin film with different Bi/Cu ratio (Figure S7); secondary electron edge, valence band edge, Cu 2P and Bi 4f XPS spectra of CuO and CBO (1.97) (Figure S8); Tauc plot of CuO and CBO (1.97) thin films (Figure S9) (PDF)

■ AUTHOR INFORMATION

Corresponding Author

*E-mail: jkcooper@lbl.gov.

ORCID

Weihua Han: 0000-0002-9313-0749

Erqin Xie: 0000-0001-5647-6938

Jason K. Cooper: 0000-0002-7953-4229

Notes

The authors declare no competing financial interest.

■ ACKNOWLEDGMENTS

This material is based upon work performed by the Joint Center for Artificial Photosynthesis, a DOE Energy Innovation Hub, supported through the Office of Science of U.S. Department of Energy under Award DE-SC0004993. EDX mapping was performed at the Molecular Foundry, supported by the Office of Science, Office of Basic Energy Science, of the U.S. Department of Energy under Contract DE-AC02-05CH11231. ZZ would also like to acknowledge the Chinese Scholarship Council (CSC) for providing funding.

■ REFERENCES

(1) Sahoo, P. P.; Zoellner, B.; Maggard, P. A. Optical, electronic, and photoelectrochemical properties of the p-type Cu3−xVO4 semiconductor. *J. Mater. Chem. A* **2015**, *3*, 4501−4509.

(2) Lalanne, M.; Barnabe, A.; Mathieu, F.; Tailhades, P. Synthesis and thermostructural studies of a CuFe(1-x)Cr(x)O(2) delafossite solid solution with 0 < or= x < or= 1. *Inorg. Chem.* **2009**, *48*, 6065−6071.

(3) Sullivan, I.; Sahoo, P. P.; Fuoco, L.; Hewitt, A. S.; Stuart, S.; Dougherty, D.; Maggard, P. A. Cu-Deficiency in the p-Type Semiconductor Cu5−xTa11O30: Impact on Its Crystalline Structure, Surfaces, and Photoelectrochemical Properties. *Chem. Mater.* **2014**, *26*, 6711−6721.

(4) Jang, Y. J.; Park, Y. B.; Kim, H. E.; Choi, Y. H.; Choi, S. H.; Lee, J. S. Oxygen-Intercalated CuFeO2 Photocathode Fabricated by Hybrid Microwave Annealing for Efficient Solar Hydrogen Production. *Chem. Mater.* **2016**, *28*, 6054−6061.

(5) Joshi, U. A.; Maggard, P. A. CuNb3O8: A p-Type Semiconducting Metal Oxide Photoelectrode. *J. Phys. Chem. Lett.* **2012**, *3*, 1577−1581.

(6) Minami, T.; Nishi, Y.; Miyata, T. High-Efficiency Cu2O-Based Heterojunction Solar Cells Fabricated Using a Ga2O3Thin Film as N-Type Layer. *Appl. Phys. Express* **2013**, *6*, 044101.

(7) Das, B.; Renaud, A.; Volosin, A. M.; Yu, L.; Newman, N.; Seo, D. K. Nanoporous delafossite CuAlO2 from inorganic/polymer double gels: a desirable high-surface-area p-type transparent electrode material. *Inorg. Chem.* **2015**, *54*, 1100−1108.

(8) Luo, J.; Steier, L.; Son, M. K.; Schreier, M.; Mayer, M. T.; Gratzel, M. Cu2O Nanowire Photocathodes for Efficient and Durable Solar Water Splitting. *Nano Lett.* **2016**, *16*, 1848−1857.

(9) Sullivan, I.; Zoellner, B.; Maggard, P. A. Copper(I)-Based p-Type Oxides for Photoelectrochemical and Photovoltaic Solar Energy Conversion. *Chem. Mater.* **2016**, *28*, 5999−6016.

(10) Kang, D.; Hill, J. C.; Park, Y.; Choi, K.-S. Photoelectrochemical Properties and Photostabilities of High Surface Area CuBi2O4and Ag-Doped CuBi2O4Photocathodes. *Chem. Mater.* **2016**, *28*, 4331−4340.

(11) Cao, D.; Nasori, N.; Wang, Z.; Mi, Y.; Wen, L.; Yang, Y.; Qu, S.; Wang, Z.; Lei, Y. p-Type CuBi2O4: an easily accessible photocathodic material for high-efficiency water splitting. *J. Mater. Chem. A* **2016**, *4*, 8995−9001.

(12) Yang, J.; Du, C.; Wen, Y.; Zhang, Z.; Cho, K.; Chen, R.; Shan, B. Enhanced photoelectrochemical hydrogen evolution at p-type CuBi 2 O 4 photocathode through hypoxic calcination. *Int. J. Hydrogen Energy* **2018**, *43*, 9549−9557.

(13) Li, J.; Griep, M.; Choi, Y.; Chu, D. Photoelectrochemical overall water splitting with textured CuBi2O4 as a photocathode. *Chem. Commun. (Cambridge, U. K.)* **2018**, *54*, 3331−3334.

(14) Berglund, S. P.; Lee, H. C.; Nunez, P. D.; Bard, A. J.; Mullins, C. B. Screening of transition and post-transition metals to incorporate into copper oxide and copper bismuth oxide for photoelectrochemical hydrogen evolution. *Phys. Chem. Chem. Phys.* **2013**, *15*, 4554−65.

(15) Lahmar, H.; Benamira, M.; Akika, F. Z.; Trari, M. Reduction of chromium (VI) on the hetero-system CuBi 2 O 4 /TiO 2 under solar light. *J. Phys. Chem. Solids* **2017**, *110*, 254−259.

(16) Guo, F.; Shi, W.; Wang, H.; Huang, H.; Liu, Y.; Kang, Z. Fabrication of a CuBi2O4/g-C3N4 p−n heterojunction with enhanced visible light photocatalytic efficiency toward tetracycline degradation. *Inorg. Chem. Front.* **2017**, *4*, 1714−1720.

(17) Nishikawa, M.; Yuto, S.; Hasegawa, T.; Shiroishi, W.; Honghao, H.; Nakabayashi, Y.; Nosaka, Y.; Saito, N. Compositing effects of CuBi 2 O 4 on visible-light responsive photocatalysts. *Mater. Sci. Semicond. Process.* **2017**, *57*, 12−17.

(18) Zhu, L.; Basnet, P.; Larson, S. R.; Jones, L. P.; Howe, J. Y.; Tripp, R. A.; Zhao, Y. Visible Light-Induced Photoeletrochemical and Antimicrobial Properties of Hierarchical CuBi2O4by Facile Hydrothermal Synthesis. *ChemistrySelect* **2016**, *1*, 1518−1524.

(19) Sharma, G.; Zhao, Z.; Sarker, P.; Nail, B. A.; Wang, J.; Huda, M. N.; Osterloh, F. E. Electronic structure, photovoltage, and photocatalytic hydrogen evolution with p-CuBi2O4nanocrystals. *J. Mater. Chem. A* **2016**, *4*, 2936−2942.

(20) Jiang, C. M.; Segev, G.; Hess, L. H.; Liu, G.; Zaborski, G.; Toma, F. M.; Cooper, J. K.; Sharp, I. D. Composition-Dependent Functionality of Copper Vanadate Photoanodes. *ACS Appl. Mater. Interfaces* **2018**, *10*, 10627−10633.

(21) Abdi, F. F.; Berglund, S. P. Recent developments in complex metal oxide photoelectrodes. *J. Phys. D: Appl. Phys.* **2017**, *50*, 193002.

(22) Wang, F.; Septina, W.; Chemseddine, A.; Abdi, F. F.; Friedrich, D.; Bogdanoff, P.; van de Krol, R.; Tilley, S. D.; Berglund, S. P. Gradient Self-Doped CuBi2O4 with Highly Improved Charge Separation Efficiency. *J. Am. Chem. Soc.* **2017**, *139*, 15094−15103.

(23) Berglund, S. P.; Abdi, F. F.; Bogdanoff, P.; Chemseddine, A.; Friedrich, D.; van de Krol, R. Comprehensive Evaluation of

DOI: 10.1021/acsaem.9b00297
ACS Appl. Energy Mater. XXXX, XXX, XXX−XXX

CuBi2O4as a Photocathode Material for Photoelectrochemical Water Splitting. *Chem. Mater.* **2016**, *28*, 4231−4242.
(24) Wang, F.; Chemseddine, A.; Abdi, F. F.; van de Krol, R.; Berglund, S. P. Spray pyrolysis of CuBi2O4 photocathodes: improved solution chemistry for highly homogeneous thin films. *J. Mater. Chem. A* **2017**, *5*, 12838−12847.
(25) Zhang, F. X.; Saxena, S. K. Raman studies of Bi2CuO4 at high pressures. *Appl. Phys. Lett.* **2006**, *88*, 141926.
(26) Loper, P.; Moon, S. J.; de Nicolas, S. M.; Niesen, B.; Ledinsky, M.; Nicolay, S.; Bailat, J.; Yum, J. H.; De Wolf, S.; Ballif, C. Organic-inorganic halide perovskite/crystalline silicon four-terminal tandem solar cells. *Phys. Chem. Chem. Phys.* **2015**, *17*, 1619−1629.
(27) Schroder, D. K.; Thomas, R. N.; Swartz, J. C. Free Carrier Absorption in Silicon. *IEEE J. Solid-State Circuits* **1978**, *13*, 180−187.
(28) Chen, Z.; Jaramillo, T. F.; Deutsch, T. G.; Kleiman-Shwarsctein, A.; Forman, A. J.; Gaillard, N.; Garland, R.; Takanabe, K.; Heske, C.; Sunkara, M.; McFarland, E. W.; Domen, K.; Miller, E. L.; Turner, J. A.; Dinh, H. N. Accelerating materials development for photoelectrochemical hydrogen production: Standards for methods, definitions, and reporting protocols. *J. Mater. Res.* **2010**, *25*, 3−16.
(29) Hisatomi, T.; Dotan, H.; Stefik, M.; Sivula, K.; Rothschild, A.; Gratzel, M.; Mathews, N. Enhancement in the performance of ultrathin hematite photoanode for water splitting by an oxide underlayer. *Adv. Mater.* **2012**, *24*, 2699−2702.
(30) Rettie, A. J.; Chemelewski, W. D.; Emin, D.; Mullins, C. B. Unravelling Small-Polaron Transport in Metal Oxide Photoelectrodes. *J. Phys. Chem. Lett.* **2016**, *7*, 471−479.
(31) Kayes, B. M.; Atwater, H. A.; Lewis, N. S. Comparison of the device physics principles of planar and radial p−n junction nanorod solar cells. *J. Appl. Phys.* **2005**, *97*, 114302.
(32) Kannan, B.; Castelino, K.; Majumdar, A. Design of Nanostructured Heterojunction Polymer Photovoltaic Devices. *Nano Lett.* **2003**, *3*, 1729−1733.
(33) Foussekis, M.; Baski, A. A.; Reshchikov, M. A. Comparison of surface photovoltage behavior for n-type versus p-type GaN. *J. Vac. Sci. Technol., B: Nanotechnol. Microelectron.: Mater., Process., Meas., Phenom.* **2011**, *29*, 041205.
(34) Hess, L. H.; Cooper, J. K.; Loiudice, A.; Jiang, C.-M.; Buonsanti, R.; Sharp, I. D. Probing interfacial energetics and charge transfer kinetics in semiconductor nanocomposites: New insights into heterostructured TiO2/BiVO4 photoanodes. *Nano Energy* **2017**, *34*, 375−384.
(35) Kraut, E. A.; Grant, R. W.; Waldrop, J. R.; Kowalczyk, S. P. Semiconductor core-level to valence-band maximum binding-energy differences: Precise determination by x-ray photoelectron spectroscopy. *Phys. Rev. B: Condens. Matter Mater. Phys.* **1983**, *28*, 1965−1977.

DOI: 10.1021/acsaem.9b00297
ACS Appl. Energy Mater. XXXX, XXX, XXX−XXX